

Wavefield and AVO modeling using elastic thin-slab method

Xian-Yun Wu¹ and Ru-Shan Wu²

ABSTRACT

We propose a dual-domain, one-way, elastic thin-slab method for fast and accurate amplitude variation with offset (AVO) modeling. In this method, the wavefield propagates in the wavenumber domain and interacts with heterogeneity in the space domain. The approach requires much less memory and is two to three orders of magnitude faster than a full-wave method using finite difference or finite element. The thin-bed AVO and AVOs with lateral parameter variations have been conducted using the thin-slab method and compared with reflectivity and finite-difference methods, respectively. It is shown that the thin-slab method can be used to accurately model reflections for most sedimentary rocks that have intermediate parameter perturbations ($< 20\%$ for P-wave velocity and $< 40\%$ for S-wave velocity). The combined effects of overburden structure and the scattering associated with heterogeneities on AVO have been investigated using the thin-slab method. Properties of the target zone and overburden structure control the AVO trends at overall offsets. Scattering associated with heterogeneities increases local variance in the reflected amplitudes and becomes significant for the sedimentary models with weak reflections. Interpretation of AVO observations based on homogeneous elastic models would therefore bias the estimated properties of the target. Furthermore, these effects can produce different apparent AVO trends in different offset ranges.

INTRODUCTION

Amplitude variation with offset (AVO) analysis plays an important role in modern seismic data interpretation. The ultimate goal of AVO analysis is to extract in-situ elastic parameters and fluid contents from the seismic reflectivity of the target intervals. However, the observed reflection responses of a seismic target are significantly affected by many other factors, such as data collection, data process-

ing, and wave-propagation effects. Before analyzing the AVO responses, these effects should be studied and compensated.

Forward modeling can be useful in understanding wave-propagation effects on AVOs. In addition, forward modeling can also be useful in interpreting complicated AVO measurements, providing appropriate model parameters for seismic data processing, and developing algorithms of frequency-dependent AVO inversion and amplitude-preserving prestack migration (Dey-Sarkar and Svatek, 1993). Many forward-modeling algorithms are available that vary in accuracy and computational requirements.

The reflectivity method is one of the most common methods used for modeling AVO responses in layered media (Simmons and Backus, 1994; Wapenaar et al., 1999.) It can generate an exact AVO response in an arbitrarily layered medium. It cannot, however, be used for modeling the effects of lateral structure variations on AVO responses. Ray methods based on various approximations of the Zoeppritz equations are also very common for AVO analysis (Widess, 1973; Simmons and Backus, 1994; Bakke and Ursin, 1998.) However, in the presence of thin layers, primaries-only Zoeppritz modeling can produce incorrect results. Another intrinsic limit of the ray methods is that the methods cannot deal with frequency-dependent scattering associated with heterogeneities. A number of authors have applied pseudospectral and finite-difference methods to more sophisticated geologic models, including anelasticity, overburden structure, scattering attenuation, and anisotropy, for the purpose of investigating the effects of these factors on AVO (Chang and McMechan, 1996; Adriansyah and McMechan, 1998; Youn et al., 1998.) In principle, these methods can deal with arbitrarily complicated geologic models. However, they are very time consuming and memory demanding. They have particular difficulty in handling thin layers where fine grids must be used.

Ideal simulation methods for AVO modeling should be flexible in order to handle the various effects mentioned above and should have the advantages of fast computation speed and low memory demand to allow for implementation of a great amount of computation for adjusting model parameters. Thus, developing new, efficient AVO-modeling algorithms for complex structures is highly desirable.

Manuscript received by the Editor March 11, 2002; revised manuscript received December 20, 2005; published online August 28, 2006.

¹Formerly University of California, Santa Cruz, California; presently Upstream Research Company, ExxonMobil Corporation, 3120 Buffalo Speedway, Houston, Texas 95064. E-mail: xianyun.wu@exxonmobil.com.

²Modeling and Imaging Laboratory, IGPP, University of California, 1156 High Street, Santa Cruz, California 95064. E-mail: wrs@es.ucsc.edu.

© 2006 Society of Exploration Geophysicists. All rights reserved.

Dual-domain, elastic, one-way propagators implement wave propagation in heterogeneous media in mixed domains (space-wave-number domains) (Wu, 1994, 1996; Wild and Hudson, 1998). One-way propagators neglect wave reverberations between heterogeneities, but they correctly handle forward multiple scattering, including focusing/defocusing, diffraction, refraction, interference, and conversions (for elastic cases). Under the De Wolf approximation, one-way propagators can be used to model reflections. It is also termed the *one-return approximation*. The great advantages of these methods are the fast computation speed, often faster by two to three orders of magnitude than the full-wave finite-difference and finite-element methods, and the huge saving in memory. These methods have been applied successfully in seismic data migration for complex subsurface structures (Wu and Jin, 1997; Jin et al., 1999; Huang et al., 1999a, b), in seismic-reflection modeling (Wu, 1996; Wu and Huang, 1995), and in modeling long-range, crustal-wave propagation in heterogeneous waveguides to study the propagation and scattering of regional phases such as *Lg*-waves (SH-wave screen propagators) (Wu et al., 2000a, b; Wu and Wu, 2001). One-way elastic propagators are derived by Wu (1994, 1996). Wild and Hudson (1998) rederive the formulation using a geometrical reflection/transmission approach. The propagators are applied to model reflections by Xie and Wu (2001) and Wu and Wu (1999). More recently, this method has been applied to elastic prestack depth migration by Xie and Wu (2005).

In this paper, we apply the dual-domain, one-way, elastic thin-slab method to AVO modeling in sedimentary rocks. Several numerical experiments, including reflection-coefficient calculations, reflection synthetics with lateral parameter variations, and thin-bed AVO, were conducted and compared with reflectivity and finite-difference methods, respectively. The accuracy and wide-angle capacity of the thin-slab method have been demonstrated. Results that show the effects of lateral structure variations and heterogeneities on AVO in sedimentary rocks are obtained and analyzed.

ELASTIC THIN-SLAB PROPAGATORS

Wu (1994, 1996) derives the elastic thin-slab propagators for calculating forward- and backward-scattered fields by a heterogeneous thin slab using the elastic-wave Rayleigh integrals and Born scatter-

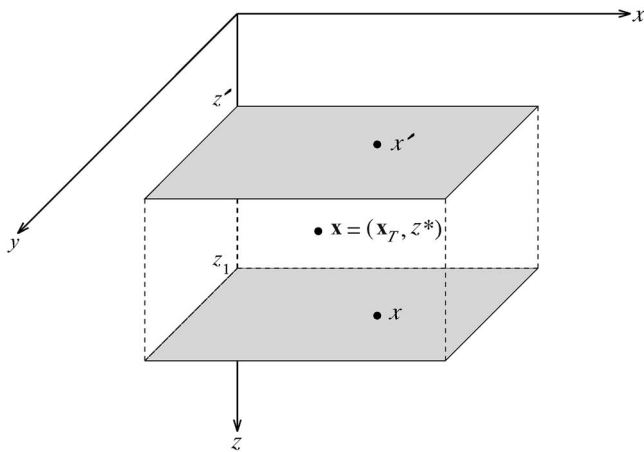


Figure 1. Illustration of a thin slab.

ing theory. In Wu (1994), the thin-slab propagators are formulated in a wavenumber domain. The interaction between the incident wavefield and the heterogeneities is in the form of matrix multiplication, which is rather computationally intensive. In Wu (1996), the thin-slab propagators are reformulated into a form of dual-domain implementation and extended to the calculation to include the backscattered waves using the De Wolf approximation. This dual-domain form of the thin-slab propagators is similar to the complex screen propagators in implementation, i.e., with propagation in the wavenumber domain using a constant background velocity, but interaction with the medium in space domain. The algorithm shuttles between the two domains using fast Fourier transform (FFT). Wu and Wu (1999) develop a fast implementation of the thin-slab propagators and test its validity and accuracy. In this paper, we adopt the formulations used in Wu and Wu (1999). A phase-matching procedure proposed by Wu and Wu (1999) is also included.

First, we divide the whole heterogeneous medium into a pile of thin slabs perpendicular to the main propagation direction or z -direction. Assume z' and z_1 as the slab entrance (top) and exit (bottom), respectively (see Figure 1). The elastic parameters and the total wavefield are decomposed into $\rho(\mathbf{x}) = \rho_0 + \delta\rho(\mathbf{x})$, $\mathbf{c}(\mathbf{x}) = \mathbf{c}_0 + \delta\mathbf{c}(\mathbf{x})$, and $\mathbf{u}(\mathbf{x}) = \mathbf{u}^0(\mathbf{x}) + \mathbf{U}(\mathbf{x})$, where ρ_0 and \mathbf{c}_0 are density and elastic parameters for the background medium, $\delta\rho(\mathbf{x})$ and $\delta\mathbf{c}(\mathbf{x})$ are the corresponding perturbations, $\mathbf{u}^0(\mathbf{x})$ and $\mathbf{U}(\mathbf{x})$ are the incident field and the scattered field, respectively, and \mathbf{x} represents a 3D spatial vector. In this study, $\mathbf{c}(\mathbf{x})$ is limited to be isotropic and heterogeneous. For the completeness of the method, we present a brief derivation of the scattered field by the heterogeneity within a slab in Appendix A.

The scattered fields \mathbf{u}^{PP} , \mathbf{u}^{PS} , \mathbf{u}^{SP} , and \mathbf{u}^{SS} obtained in Appendix A are not efficient for numerical calculation because the integral with respect to z cannot be implemented with FFT. Furthermore, we assume that each heterogeneous thin slab is thin enough so that velocity and density can be approximated as constants in the propagation direction, and the scattered fields can be simplified into

$$\begin{aligned}
 \mathbf{U}^P(\mathbf{K}_T, z^*) &= \frac{ik_\alpha^2}{2\gamma_\alpha} e^{i\gamma_\alpha \Delta z/2} \Delta z \hat{k}_\alpha \left\{ \hat{k}_\alpha \cdot \iint d^2\mathbf{x}_T e^{-i\mathbf{K}_T \cdot \mathbf{x}_T} \right. \\
 &\quad \times \frac{\delta\rho(\mathbf{x}_T, z')}{\rho} [\eta^{PP} \mathbf{u}_\alpha^f(\mathbf{x}_T) + \eta^{SP} \mathbf{u}_\beta^f(\mathbf{x}_T)] \\
 &\quad - \iint d^2\mathbf{x}_T e^{-i\mathbf{K}_T \cdot \mathbf{x}_T} \frac{\delta\lambda(\mathbf{x}_T, z')}{\lambda + 2\mu} \frac{1}{ik_\alpha} \\
 &\quad \times \nabla \cdot [\eta^{PP} \mathbf{u}_\alpha^f(\mathbf{x}_T)] - (\hat{k}_\alpha \hat{k}_\alpha) : \\
 &\quad \times \iint d^2\mathbf{x}_T e^{-i\mathbf{K}_T \cdot \mathbf{x}_T} \frac{2\delta\mu(\mathbf{x}_T, z')}{\lambda + 2\mu} \frac{1}{ik_\alpha} \\
 &\quad \left. \times [\eta^{PP} \boldsymbol{\varepsilon}_\alpha^f(\mathbf{x}_T) + \eta^{SP} \boldsymbol{\varepsilon}_\beta^f(\mathbf{x}_T)] \right\}, \quad (1)
 \end{aligned}$$

$$\begin{aligned}
\mathbf{U}^S(\mathbf{K}_T, z^*) &= \frac{ik_\beta^2}{2\gamma_\beta} e^{i\gamma_\beta \Delta z/2} \Delta z (\mathbf{I} - \hat{k}_\beta \hat{k}_\beta) \cdot \left\{ \iint d^2 \mathbf{x}_T \right. \\
&\times e^{-i\mathbf{K}_T \cdot \mathbf{x}_T} \frac{\delta \rho(\mathbf{x}_T, z')}{\rho} [\eta^{PS} \mathbf{u}_\alpha^f(\mathbf{x}_T) + \eta^{SS} \mathbf{u}_\beta^f(\mathbf{x}_T)] \\
&- \hat{k}_\beta \cdot \iint d^2 \mathbf{x}_T e^{-i\mathbf{K}_T \cdot \mathbf{x}_T} 2 \frac{\delta \mu(\mathbf{x}_T, z')}{\mu} \frac{1}{ik_\beta} \\
&\left. \times [\eta^{PS} \varepsilon_\alpha^f(\mathbf{x}_T) + \eta^{SS} \varepsilon_\beta^f(\mathbf{x}_T)] \right\}. \quad (2)
\end{aligned}$$

In equations 1 and 2, \mathbf{I} is the unit dyadic. Its diagonal elements are equal to 1, and other elements are equal to zero. The displacement, $\mathbf{u}_\alpha^f(\mathbf{x})$, $\mathbf{u}_\beta^f(\mathbf{x})$, $\nabla \cdot \mathbf{u}_\alpha^f(\mathbf{x})$ (divergence), and $\varepsilon_\alpha^f(\mathbf{x})$ and $\varepsilon_\beta^f(\mathbf{x})$ (strain) can be calculated by

$$\mathbf{u}_\alpha^f(\mathbf{x}) = \frac{1}{2\pi} \iint d^2 \mathbf{K}'_T e^{i\mathbf{K}'_T \cdot \mathbf{x}_T} \mathbf{u}_\alpha^0(\mathbf{K}'_T) e^{i\gamma'_\alpha \Delta z/2}, \quad (3)$$

$$\mathbf{u}_\beta^f(\mathbf{x}) = \frac{1}{2\pi} \iint d^2 \mathbf{K}'_T e^{i\mathbf{K}'_T \cdot \mathbf{x}_T} \mathbf{u}_\beta^0(\mathbf{K}'_T) e^{i\gamma'_\beta \Delta z/2}, \quad (4)$$

$$\nabla \cdot \mathbf{u}_\alpha^f(\mathbf{x}) = \frac{ik_\alpha}{2\pi} \iint d^2 \mathbf{K}'_T e^{i\mathbf{K}'_T \cdot \mathbf{x}_T} \hat{k}'_\alpha \cdot \mathbf{u}_\alpha^0(\mathbf{K}'_T) e^{i\gamma'_\alpha \Delta z/2}, \quad (5)$$

$$\varepsilon_\alpha^f(\mathbf{x}) = \frac{ik_\alpha}{2\pi} \iint d^2 \mathbf{K}'_T e^{i\mathbf{K}'_T \cdot \mathbf{x}_T} \hat{k}'_\alpha \mathbf{u}_\alpha^0(\mathbf{K}'_T) e^{i\gamma'_\alpha \Delta z/2}, \quad (6)$$

$$\begin{aligned}
\varepsilon_\beta^f(\mathbf{x}) &= \frac{ik_\beta}{2\pi} \iint d^2 \mathbf{K}'_T e^{i\mathbf{K}'_T \cdot \mathbf{x}_T} \frac{1}{2} [\hat{k}'_\beta \mathbf{u}_\beta^0(\mathbf{K}'_T) \\
&+ \mathbf{u}_\beta^0(\mathbf{K}'_T) \hat{k}'_\beta] e^{i\gamma'_\beta \Delta z/2}, \quad (7)
\end{aligned}$$

where \mathbf{x}_T is the horizontal position in the receiver plane at z^* ($z' \leq z^* \leq z_1$). γ_α and γ_β are the vertical components of wavenumbers of scattered P- and S-waves, and γ'_α and γ'_β are the vertical components of wavenumbers of incident P- and S-waves. The values $k_\alpha = \omega/\alpha_0$ and $k_\beta = \omega/\beta_0$ are P and S wavenumbers, respectively, and α_0 and β_0 are P- and S-wave velocities in the background medium. Terms λ and μ are the Lamé constants, and $\delta\lambda$ and $\delta\mu$ are the corresponding perturbations. Terms \hat{k}_α , \hat{k}_β , \hat{k}'_α , and \hat{k}'_β are unit wavenumber vectors: $\hat{k}_\alpha = (\mathbf{K}_T, \gamma_\alpha)/k_\alpha$, $\hat{k}_\beta = (\mathbf{K}_T, \gamma_\beta)/k_\beta$, $\hat{k}'_\alpha = (\mathbf{K}'_T, \gamma'_\alpha)/k_\alpha$, $\hat{k}'_\beta = (\mathbf{K}'_T, \gamma'_\beta)/k_\beta$. $\mathbf{u}_\alpha^0(\mathbf{K}'_T)$ and $\mathbf{u}_\beta^0(\mathbf{K}'_T)$ are the incident P- and S-wave displacements at the entrance $z = z'$, respectively. $\mathbf{A} \cdot$ denotes dot product between vectors, and \cdot denotes double dot product between tensors. Values $\iint d^2 \mathbf{x}_T$ and $\iint d^2 \mathbf{K}'_T$ denote dual integrals over spatial and wavenumber domains. The Fourier transform can be implemented with the FFT technique; $\Delta z = z_1 - z'$ is the thin-slab thickness. The factors η^{PP} , $\eta^{SP} = \eta^{PS}$, and η^{SS} are

$$\begin{aligned}
\eta^{PP} &= \begin{cases} 1 & \text{for focusscattering} \\ \text{sinc}(k_\alpha \Delta z) & \text{for backscattering} \end{cases} \\
\eta^{PS} &= \begin{cases} \text{sinc}[(k_\alpha - k_\beta) \Delta z/2] & \text{for focusscattering} \\ \text{sinc}[(k_\alpha + k_\beta) \Delta z/2] & \text{for backscattering} \end{cases}
\end{aligned}$$

$$\eta^{SS} = \begin{cases} 1 & \text{for focusscattering} \\ \text{sinc}(k_\beta \Delta z) & \text{for backscattering} \end{cases}$$

where $\text{sinc}(x) = \sin(x)/x$. Equations 1 and 2 describe the complex interactions between incident field and heterogeneities. The spatial scattering patterns associated with different types of perturbations ($\delta\lambda$, $\delta\mu$, and $\delta\rho$) for P- and S-waves are investigated in Wu and Aki (1985). For forward propagation, equations 1 and 2 can handle all forward multiple scattering, including focusing/defocusing, diffraction, interference, and conversions. For backward propagation, it can handle primary reflections of common-type waves and converted waves.

The thin-slab method is a marching algorithm. The whole medium is sliced into appropriate thin slabs perpendicular to the main propagation direction. A weak scattering condition holds for each thin slab, and the parameters can be considered invariable within each thin slab in the main propagation direction. Suppose all incident fields at the entrance of each thin slab are given in wavenumber domain. The implementation procedures may be summarized as follows:

- Free-propagate in wavenumber domain and calculate the primary fields, the divergence of incident P-wave, and the strains.
- Inverse FFT the primary fields, divergence, and strains into space domain, and then calculate the distorted fields by heterogeneities.
- Calculate the focusscattered fields at the thin-slab exit and backscattered fields at the thin-slab entrance, and add the focusscattered fields to the primary fields to form the total fields being used as incident fields for the next thin slab.
- Continue these three procedures iteratively until the last thin slab, and generate total transmitted fields.
- Repeat the first three procedures from the last thin slab to the first one and sum up all backscattered fields generated by each thin slab to get the total reflected fields.

In the thin-slab solution, the effect of free surface is not involved. In other words, the background medium is assumed to be infinite in all directions. The medium where source is located is usually taken as the background medium to avoid strong wave-slab interaction at the near-source region. A Ricker wavelet centered at 30 Hz is used in synthesizing seismograms. Only vertical displacement seismograms are shown in all examples, unless noted otherwise.

RESERVOIR PROPERTIES

Table 1 shows the rock properties used in this paper, which are taken from Simmons and Backus (1994) (originally from Gregory, 1977). The reservoir contains brine, oil, and gas. The behavior of the shale/gas, shale/oil, shale/brine, and fluid-contact reflections as functions of incident angle and porosity are of interest. Garcia and Backus (1985) also examine the AVO responses of these models. Simmons and Backus (1994) investigate the effects of locally converted shear waves on AVO responses of the same models. The reservoirs correspond to the sedimentary rocks, which are of low velocity and density perturbations but have large changes in Poisson's ratio from one medium to another (Table 1). In all our examples, the shale is taken as the background medium. Gas, oil, and brine sands are taken to have different velocity and density perturbations relative to the shale (Table 2). Two-dimensional random perturbations are introduced to the models for analyzing the effect of scattering by random heterogeneities in overburden on AVO.

NUMERICAL EXAMPLES AND DISCUSSION

Reflection coefficients

Reflection coefficients vary as a function of offset because of elastic parameter changes across an interface. This information is the core of AVO analysis. For either forward modeling or inversion, accurate prediction and estimate of reflection coefficients are crucial.

The accuracy and wide-angle capacity of the thin-slab method are tested in Wu and Wu (1999). For the general purpose of the test, the paper focuses only on relatively weak changes in P- and S-wave velocities and density across the reflecting interface ($<20\%$) and considered only Poisson's formation ($\sigma = 0.25$). However, sedimentary reservoirs bearing gas, oil, or brine presented above have large changes, up to 42.3% in velocity and up to 70% in Poisson's ratio.

In this section, we calculate the reflection coefficients at the shale/gas, shale/oil, and shale/brine interfaces, respectively, with parameters given in Table 1 using the thin-slab method and show the ability of the method to handle these models. For the calculation using equations 1 and 2, a model space is defined on a 1024×200 rectangular grid. The grid spacings used are 16 m in the horizontal direction and 4 m in the vertical direction. The interface is located at 200 m depth. A taper function is applied to the bottom of the model to eliminate the reflection from the bottom. Only P-P reflection coefficients are displayed. For reflection-coefficient calculation, we take 200 samples (displacement amplitudes in space domain) in the middle of the model for incident waves and reflected waves, respectively, to avoid the edge effects, and define the ratio of the averaged displacement amplitudes of the reflected wave to the incident wave as reflection coefficient. Figure 2 shows the P-P reflection coefficients for all sets of parameters given in Table 1. The dotted curves represent the corresponding theoretical results, ϕ is percentage porosity, and σ_1 and σ_2 are the Poisson's ratios for the shale and sand, respectively. Figure 2a corresponds to the shale/gas interface, Figure 2b

corresponds to the shale/oil interface, and Figure 2c corresponds to shale/brine interface. We see that the reflection coefficients calculated by the thin-slab method are in good agreement with theoretical values for small and medium angles of incidence ($<30^\circ$) for all cases, and up to wide angle of incidence ($<40^\circ$) for the 20% porosity gas, oil, and brine sands.

Although the 20% porosity sand has relatively large velocity perturbations, the thin-slab results show better matches to theoretical reflection coefficients in wide angles of incidence than those for 23% porosity and 25% porosity sands in wide angles. This is because for reflections, accuracy is controlled by impedance perturbations, which are small in these cases.

The computational efficiency, accuracy, and wide-angle capacity of the thin-slab method are closely related to the amount of perturbations. Generally, the accuracy and wide-angle capacity decrease as perturbations (velocity and/or density) increase. Its computational efficiency also decreases because finer forward steps must be utilized for convergence. To see the overall perturbations of reservoir parameters shown in Table 1, we calculate velocity and density fluctuations relative to the shale (shown in Table 2). For all models, S-wave velocity has relatively large contrasts compared with P-wave velocity and density. For example, the averaged S-wave velocity perturbations are 38.2% for 20% porosity sand, 29.3% for 23% porosity sand, and 22.6% for 25% porosity sand, while the averaged P-wave velocity perturbations are 16% for 20% porosity sand, 9.7% for 23% porosity sand, and 4.6% for 25% porosity sand. As to parameter perturbations, Table 2 covers most sedimentary rocks.

Reflections from a dipping sandstone reservoir

Figure 3 shows a model of a dipping sandstone reservoir bearing gas, oil, and brine. The dipping angle of the reservoir is 10° to the horizontal plane. The reservoir is thick enough so that the reflections

Table 1. Reservoir model.

	$\phi = 20\%$				$\phi = 23\%$				$\phi = 25\%$			
	α m/s	β m/s	ρ g/cm ³	σ	α m/s	β m/s	ρ g/cm ³	σ	α m/s	β m/s	ρ g/cm ³	σ
Shale	3170	1668	2.36	0.31	3170	1668	2.36	0.31	3170	1668	2.36	0.31
Gas	3560	2374	2.10	0.10	3350	2231	2.02	0.10	3188	2124	1.96	0.10
Oil	3734	2280	2.27	0.20	3527	2131	2.22	0.21	3362	2015	2.18	0.22
Brine	3749	2262	2.31	0.21	3551	2109	2.27	0.23	3399	1993	2.23	0.24

Table 2. Perturbations of reservoir parameters.

	$\phi = 20\%$				$\phi = 23\%$				$\phi = 25\%$			
	$\frac{\delta\alpha}{\alpha}$ %	$\frac{\delta\beta}{\beta}$ %	$\frac{\delta\rho}{\rho}$ %	σ	$\frac{\delta\alpha}{\alpha}$ %	$\frac{\delta\beta}{\beta}$ %	$\frac{\delta\rho}{\rho}$ %	σ	$\frac{\delta\alpha}{\alpha}$ %	$\frac{\delta\beta}{\beta}$ %	$\frac{\delta\rho}{\rho}$ %	σ
Gas	12.3	42.3	-11.0	0.10	5.7	33.7	-14.4	0.10	0.6	27.0	-17.0	0.10
Oil	17.8	36.7	-3.80	0.20	11.3	27.8	-5.9	0.21	6.1	20.8	-7.6	0.22
Brine	18.3	35.6	-2.10	0.21	12.0	26.4	-3.8	0.23	7.2	19.5	-5.5	0.24

from the top and base are separated in seismograms. Simmons and Backus (1994) use these models to investigate AVO responses associated with angles of incidence, different interfaces, and porosities of interest. In this section, we will use these models to show the accuracy of the thin-slab method for modeling reflections, including primary reflections, conversions, and diffractions.

Figure 4 displays the synthetic seismograms with incident plane waves for three different porosities (labeled left of each panel). The plane P-wave source is vertically downward incident to the model. The time function of the source used is the Ricker wavelet. Assume that the same source will be used for subsequent examples unless otherwise specified. Figure 4a shows the finite-difference results and Figure 4b shows the thin-slab results. The last two arrivals are the converted shear waves produced at the top and base of the reservoir and propagated in the shale. Single-leg and double-leg converted shear waves are weak at small angle of incidence (relative to interface) and overlap with the primary reflections from the base. Note that in the thin-slab results (Figure 4b), the multiples within the sandstone are neglected. Comparing the two columns, we see that the thin-slab results are in good agreement with the finite-difference results, implying that the multiples are not important in these kinds of sedimentary rocks.

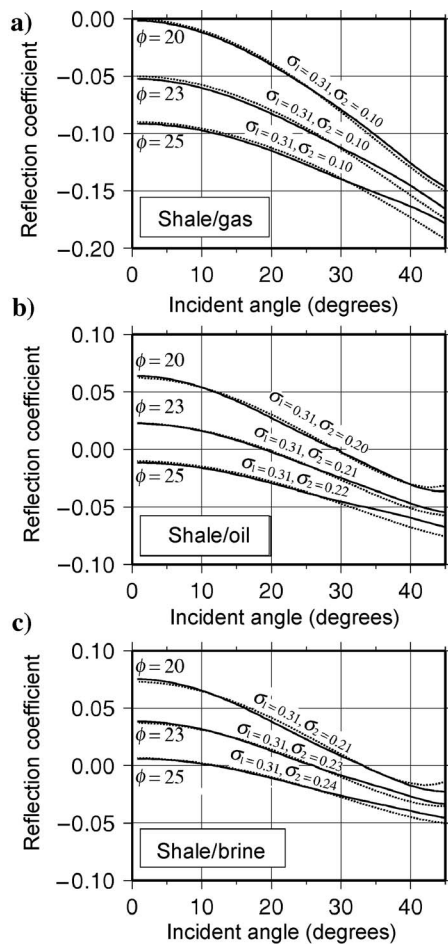


Figure 2. P - P reflection coefficients at different types of interfaces: (a) shale/gas, (b) shale/oil, and (c) shale/brine. All formation parameters are listed in Table 1. The solid curves are calculated by the thin-slab method, and the dotted ones are calculated by the Zoeppritz equations.

The diffractions in Figure 4, because of the irregularities of the model, strongly interfere with the primary reflections from the top and base interfaces, so that they cannot be distinguished. Figure 5 displays similar results to Figure 4, but the top and base interfaces of the reservoir are horizontal, and the gas/oil and oil/brine interfaces are rotated to vertical lines. Although this geometry model may not be realistic, it does not affect the conclusion of our investigation. In this case, the diffractions are well produced and can be seen in the seismograms calculated by both finite-difference and thin-slab methods. For 20% porosity gas sand, the impedance contrast at

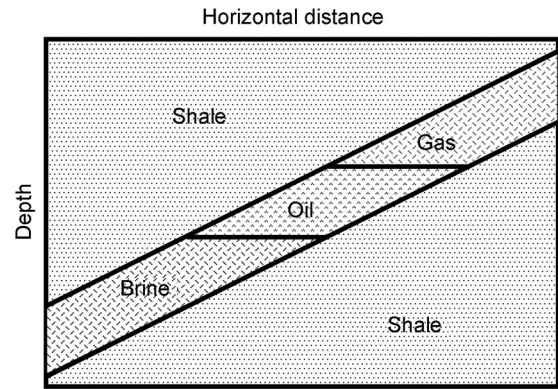


Figure 3. Model of a dipping sandstone reservoir filled with gas, oil, and brine. The reservoir is thick enough so that the reflections from the top and base are resolved.

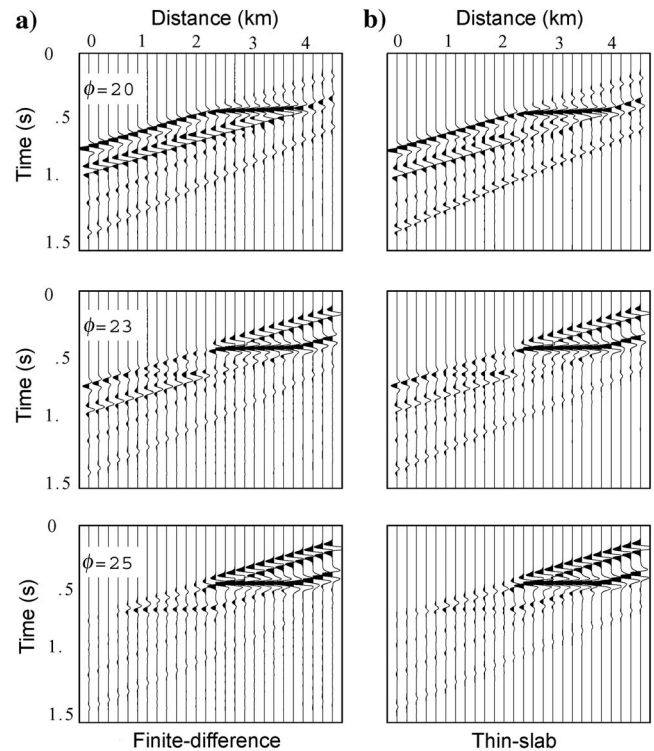


Figure 4. Comparisons of synthetic seismograms with plane-wave incidence calculated by finite-difference (a) and thin-slab methods (b) for a dipping reservoir model (Figure 3). The vertical axis is time, and the horizontal axis is distance.

shale/gas interface equals zero. That means that there are no reflections generated from the local interface for vertical incidence. The arrivals recorded by the receivers just above the shale/gas interface are the diffractions produced by the two intersectional points surrounded by shale, gas, and oil sands. We can see similar results for the 25% porosity sand.

Plane-wave reflections with random scattering

All seismic data, to varying degrees, contain the effects of scattering by the overburden heterogeneities. When variations in velocity, density, and intrinsic Q are correlated spatially in the overburden, the total amount of scattered energy increases, while local wave amplitudes may increase or decrease because of focusing/defocusing. Many seismic data sets showed these effects (see Yilmaz, 1987, 30–40). Kang and McMechan (1994) investigate the interaction of intrinsic attenuation and apparent attenuation associated with scattering. Chang and McMechan (1996) investigate the multiparameter seismic scattering by Q heterogeneities. Adriansyah and McMechan (1998) study the combined effects of near-surface geometry, intrinsic attenuation, and scattering on AVO.

In this section, we examine the effects of scattering associated with heterogeneities in sedimentary rocks on AVO using the thin-slab method. The reservoir model is similar to the one used in Figure 5, but a 2D random field with exponential correlation functions is used to perturb the velocity and density parameters of the sedimentary rocks. The correlation lengths are 100 m in horizontal direction and 40 m in depth. The root mean square (rms) values used are 1%, 2%, and 3%. Note that both P- and S-wave velocities have the same

distributions and rms perturbations, and density has the same distribution but only one half of the rms perturbation as for velocity. For simplicity, we only consider a plane P-wave source vertically incident on the top interface of the reservoir. Figure 6 shows the model and the snapshots at $t = 0.2$ s, 0.4 s, and 0.6 s, respectively. The porosity of the sand is 25% and rms is 2%. In Figure 6, we see that abundant coda waves are produced. The wavefronts of either forward-propagated or reflected waves are no longer uniform; especially for the reflections from shale/oil and shale/brine interfaces, the wavefronts are seriously distorted. Then, we take the maximum magnitudes of the responses from the top interface of the sand and display the results in Figure 7. The vertical axis is plotted in the logarithm of absolute amplitudes to better display the weak reflections. Figure 7a–c correspond to three different porosities of 20%, 23%, and 25%, respectively. Solid lines correspond to the cases without heterogeneity in the overburden, and the local fluctuations in reflected amplitudes are caused by the interference of the boundary diffractions. The dotted, dashed, and dotted-dashed ones correspond to the cases

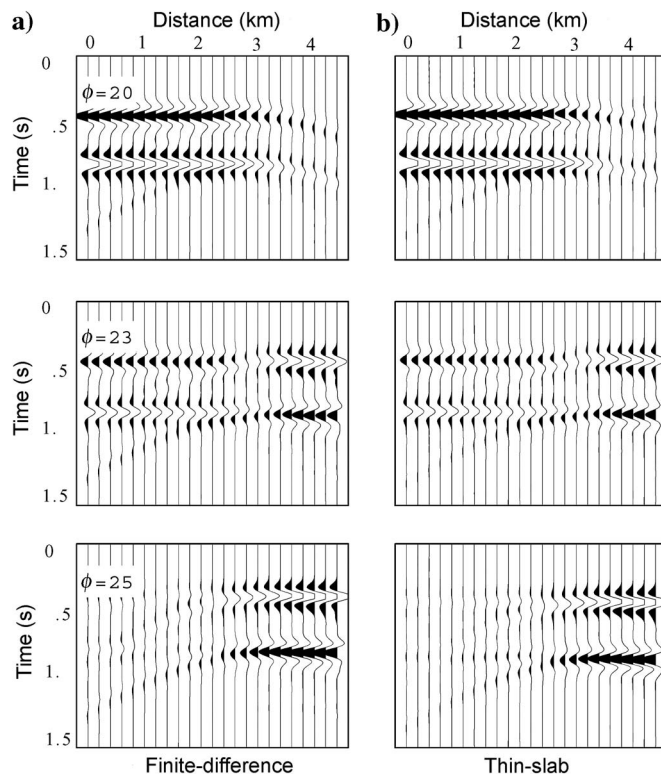


Figure 5. Comparisons of synthetic seismograms with plane-wave incidence calculated by (a) finite-difference and (b) thin-slab methods for a flat reservoir model filled with gas, oil, and brine.

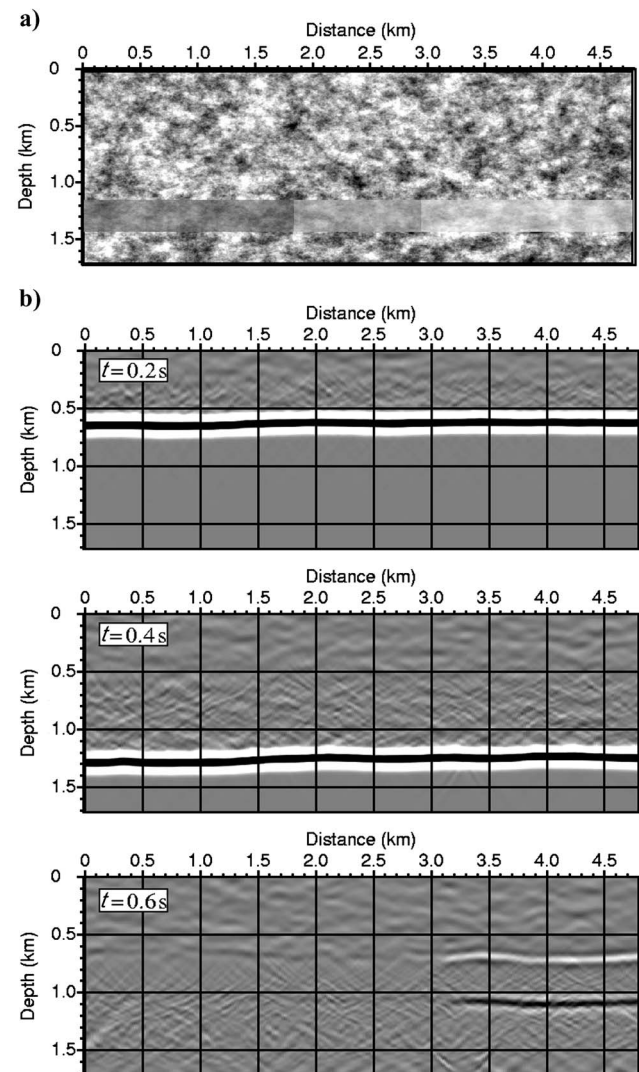


Figure 6. (a) Sandstone model with heterogeneities, (b) Snapshots at $t = 0.2$ s, 0.4 s, and 0.6 s, respectively. A 30-Hz plane P-wave source is vertically incident from the top of the model.

with the rms values of 1%, 2%, and 3%, respectively. The arrows point out the positions of vertical interfaces separating gas and oil, or oil and brine.

It is clear that when the overlying shale is heterogeneous, even as weak as rms = 1%, the piece-wise, uniform, reflected amplitudes become fluctuating by the local focusing and defocusing. As the value of rms increases, higher fluctuations will be produced. The fluctuations are closely related to the spatial correlation of heterogeneities. For an overburden with white-noise random heterogeneities, the local focusing or defocusing will not happen. We also see that the scattering associated with heterogeneities has stronger effects on the reflections from weak-reflection interfaces (shale/gas at a 20% porosity sand and shale/brine at a 25% porosity sand) than from strong-reflection interfaces (shale/brine at 20% porosity sand and shale/gas at 25% porosity sand).

We calculated the local reflection coefficients at the top interface after introducing heterogeneities to the overburden shale. These heterogeneities can affect the reflected amplitudes. This implies that the presence of heterogeneities has two effects: wave scattering and change in the reflection characteristics of local interfaces. For weak-reflection sands, the scattering effects from heterogeneous overburden could be important and must be taken into account for AVO analysis.

Thin-layer AVO response

The amplitude response of a thin bed has drawn increasing interest in hydrocarbon interpretation because large quantities of gas reserves were found to be trapped within thin sands. The AVO response of a thin bed is different from that of a thick bed because of the effects of wave interference, conversion, and tuning. Many authors discussed the amplitude responses of thin beds using ray-based methods (Widess, 1973; Simmons and Backus, 1994; Chung and Lawton, 1995; Bakke and Ursin, 1998).

Widess (1973) considers a homogeneous thin layer embedded in an infinite homogeneous medium. He shows that for a thin bed, whose thickness is less than one-eighth of the dominant wavelength, the reflected wavelet would be equivalent to the derivative of the input wavelet. The maximum amplitude of the reflection is approximately given by

$$A_d = \frac{4\pi A_m r b}{\lambda_d}, \quad (8)$$

where A_m is the mean of the maximum peak and trough amplitudes of the source wavelet, r is the reflection coefficient of the top interface corresponding to a thick layer, b is the thin-bed thickness, and λ_d is the predominant wavelength in the bed. Chung and Lawton (1995) extend Widess' work to the more general case of unequal reflection coefficients at the top and base of the bed. Simmons and Backus (1994) studied the amplitude responses of an elastic thin bed where a locally converted wave was involved. They demonstrate that the interference between the converted waves and the primary reflections from the base of the layers becomes increasingly important as layer thicknesses decrease, often producing a seismogram that is very different from one produced under the primaries-only Zoeppritz assumption.

For a thin bed whose thickness is much less than the corresponding predominant wavelength, the grid methods such as finite difference and finite element are not realistic for modeling reflections in an AVO geometry. In this section, we investigate the ability of the thin-

slab method in handling elastic thin-bed reflections. The thin bed used is a 5-m-thick sand filled with oil and at a depth of 1500 m. The corresponding predominant wavelength is 125 m, being 25 times greater than the thickness of the thin bed. The surrounding medium is shale. Source and receivers are on the top of the model. For the calculation using the thin-slab method, the spacing grid in the horizontal direction is 10 m and that in the vertical direction is 10 m for the background area, and 0.5 m for the thin bed. Figure 8 displays reflection seismograms calculated by reflectivity method (a) and thin-slab method (b). The time function of the source used is the derivative of the Ricker wavelet. Seismograms were given normal moveout (NMO) corrections to the top of the sand. In Figure 8, A represents reflections from the top of the model (thick layer); B represents reflections from both the top and base, but with no converted waves involved; C represents all waves involved (exact solution); and D represents reflections from both the top and base, involving single-leg (the wave propagates in the reservoir layer as a converted wave once only) and double-leg converted shear waves. Comparing A and B, we see the big difference between AVOs of a single impedance interface and two closely located impedance interfaces. B is equivalent to primary-only reflections. Comparing B and C/D, we see the important effect of locally converted shear waves on AVO responses, which can alter amplitude variation with offset. Comparing C and D, we see that only a small difference exists between them in large offsets. The effect of the multiples is again shown to be negligible.

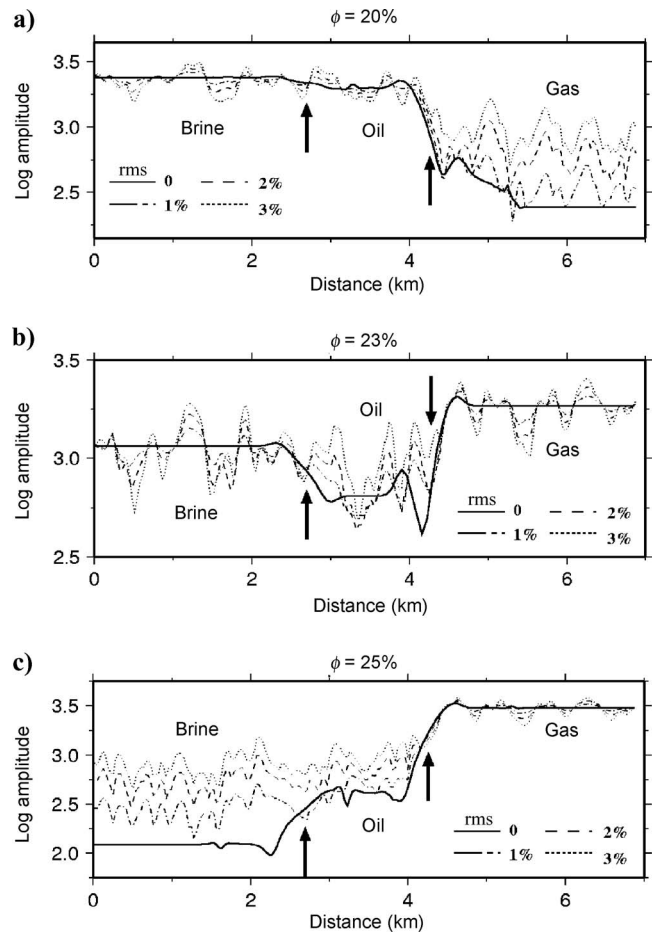


Figure 7. Effects of scattering by heterogeneities on reflected amplitudes.

For a homogeneous thin slab under small-angle approximation, equation 1 for one-return reflection can be simplified to (Wu, 1996; Xie and Wu, 2001)

$$U^P(\mathbf{K}_T) = -ik_\alpha \Delta z \frac{\delta Z_\alpha}{Z_\alpha} \mathbf{u}_\alpha^0(\mathbf{K}_T), \quad (9)$$

where Z_α is the impedance of the P-wave. We see that equation 8 is the special case of equation 9, where plane waves are vertically incident on the thin layer. Equation 9 presents not only the amplitude of the thin-bed reflection, but also the change in the wavelet. Therefore, the thin-slab propagators, i.e., equations 1 and 2, represent the response of an elastic, heterogeneous thin slab. Since the choice of Δz or step interval in wavefield extrapolation is flexible and can vary according to local heterogeneities in wave-propagation direction, the thin-slab method can handle arbitrarily thin layers.

AVO in laterally varying media

Lateral changes in the overburden properties have demonstrated significant effects on AVO and may cause misinterpretation, especially if the recording aperture is small. Adriansyah and McMechan (1998) use the pseudospectral method to investigate the combined effects of near-surface structure, attenuation, and scattering on AVO. Youn et al. (1998) investigate the effects of the overlying salt body on AVO using the finite-difference method. These methods are very time-consuming and memory-demanding.

In this section, we use a simple model containing both a truncated

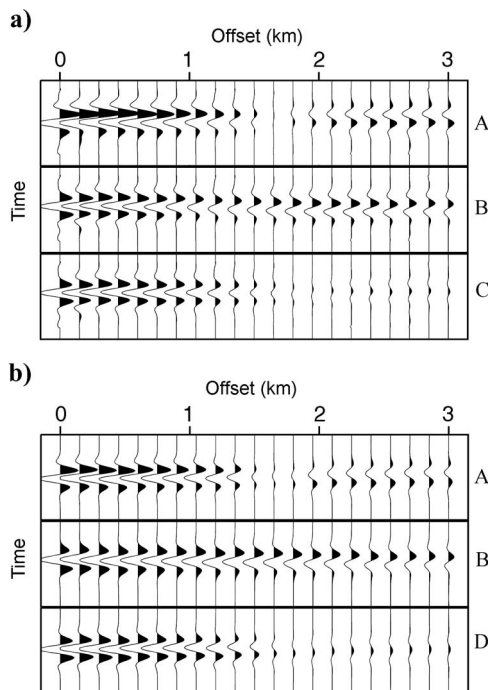


Figure 8. Reflection seismograms for an oil sand model. The oil sand is 5 m thick and at depth of 1500 m shown are (a) the reflectivity method and (b) the thin-slab method. In (a) and (b), A represents reflections from the top of the model (thick layer); B represents reflections from both the top and base, but with no converted waves involved; C represents all waves involved (exact solution); and D represents reflections from both the top and base, involving single-leg and double-leg converted shear waves.

salt layer and a thin gas sand that is 200 m below the salt layer (Figure 9a) to examine the AVO response using the thin-slab method. The parameters for gas sand are given in Table 1, and the corresponding porosity is 20%. The parameters for salt are $\alpha = 4.48$ km/s, $\beta = 2.594$ km/s, and $\rho = 2.1$ g/cm³. Thicknesses of the salt layer used are 20 m, 40 m, and 80 m, respectively. The spacing grids used are the same used in Figure 8 except for the spacing grid of the salt body in the vertical direction, where it is 0.1 m. The maximum negative amplitudes of the thin-bed responses are picked and are plotted versus offset (Figure 9b). The solid curve represents the case of a thin-bed AVO without salt. The AVO trend of a thin bed is different from the reflection-coefficient variation versus incident angle shown in Figure 2 (shale/gas, $\phi = 20$), where the reflection coefficient increases as incident angles up to 45° (the offset of 3 km). The dotted, dashed, and dotted-dashed curves correspond to different salt-layer thicknesses of 20 m, 40 m, and 80 m, respectively. We see that AVOs are altered by the presence of the salt layer. The salt layer produces the effects of diffraction, defocusing, conversion, and transmission loss. The diffraction affects AVO by causing interference between diffracted waves from the left side of the salt layer and reflected waves from the thin bed at receiver locations. It causes local changes in AVO. On the other hand, the transmission loss affects all the reflections propagating through the salt body and causes a systematic decrease in AVO.

Figure 10 shows the combined effects of a truncated salt layer and heterogeneities on AVO by introducing heterogeneities to Figure 9a. The correlation lengths of a 2D random field used are 100 m in the horizontal direction and 40 m in the vertical direction. The rms values used are 1%, 2%, and 3%, respectively. The four panels from top to bottom correspond to the cases of zero salt, and 20, 40, and

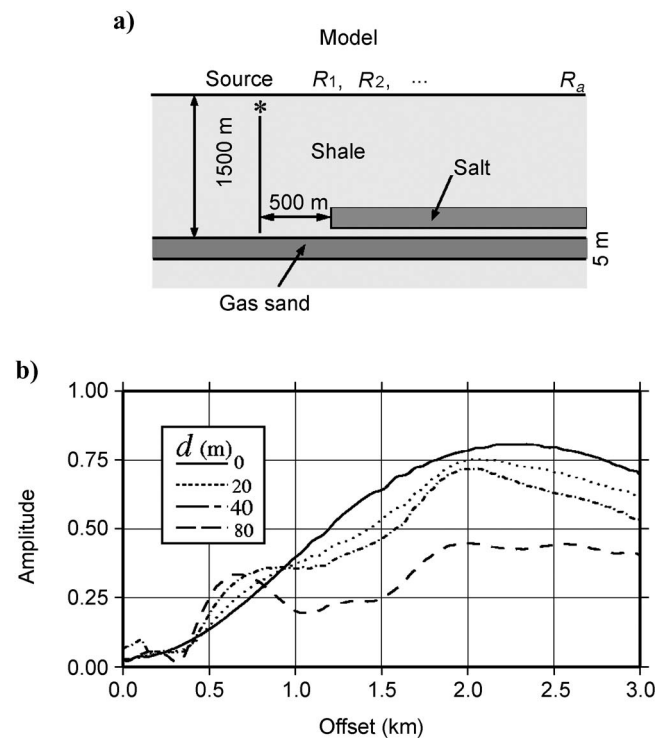


Figure 9. (a) Model containing a truncated salt layer and a thin gas sand below the salt layer. (b) AVOs of a thin gas layer with the effects of salt layer; d denotes salt-layer thickness.

80-m-thick salt, respectively. The top panel shows the effect of heterogeneities on AVO alone. The focusing and defocusing of the spatially correlated heterogeneities produce the local variation in reflected AVO values, which becomes significant for the sedimentary models with weak reflections. Interpretation of AVO observations based on homogeneous elastic models will therefore bias the estimated properties of the target. The periods and magnitude of the local variations are closely related to the frequency of source, correlation lengths, and rms of heterogeneity. While the overall AVO trends are controlled mainly by the properties of the target zone and overburden structure, these effects can produce different apparent-AVO trends in different offset ranges. It is necessary to have sufficient ap-

ertures in AVO measurement in sedimentary rocks and to take into account all of the effects of heterogeneous overburdens, including random heterogeneities and thin-beds.

CONCLUSIONS

In this paper, we present a dual-domain, one-way, elastic thin-slab method for wavefield and AVO modeling in sedimentary rocks. Numerical results show that the reverberations between heterogeneities, which are not accounted for in the thin-slab method, may be neglected in most sedimentary rocks. The wave phenomena of primary reflection, conversion, focusing/defocusing, interference, and diffraction are accurately handled by the thin-slab method. A flexible choice of step intervals in wavefield extrapolation makes the method very efficient for modeling thin-bed AVO responses, in contrast to the grid methods, which need very fine grids and therefore may become very costly.

The combined effects of overburden structure and scattering by heterogeneities on AVO of a thin bed in shale significantly alter AVO responses. Properties of the target zone and overburden structure control the AVO trends at overall offsets. These effects can produce different apparent AVO trends in different offset ranges, so it is necessary to have sufficient apertures in AVO measurement in sedimentary rocks. Scattering associated with heterogeneities increases the local variation in reflected amplitudes, which becomes significant for the sedimentary models with weak reflections. Without compensation for these effects, interpretation of AVO observations based on homogeneous elastic-medium assumption will be severely biased.

Complete compensation of wave-propagation effects would involve the effects of intrinsic attenuation and anisotropy. We are working on extending the thin-slab method to handle these cases. The effect of intrinsic attenuation of the background medium can be easily introduced into the dual-domain (space-wavenumber) method. More improvements of the thin-slab method are also needed to enhance the wide-angle accuracy and to handle large-contrast reservoirs.

ACKNOWLEDGMENTS

We would like to thank the two anonymous reviewers and the two editors for their valuable comments. This research is supported by the Department of Energy under Grant No. DE-FG03-01ER15144. Facility support from the W. M. Keck Foundation is acknowledged. Contribution No. 451 of the CSIDE, IGPP, University of California, Santa Cruz, is also acknowledged.

APPENDIX A

ELASTIC THIN-SLAB PROPAGATORS

The equation of motion in a linear, heterogeneous, elastic medium can be written as (Aki and Richards, 1980)

$$-\omega^2 \rho(\mathbf{x}) \mathbf{u}(\mathbf{x}) = \nabla \cdot \boldsymbol{\sigma}(\mathbf{x}), \quad (\text{A-1})$$

where \mathbf{u} is the displacement vector, $\boldsymbol{\sigma}(\mathbf{x})$ is the stress tensor (dyadic), and ρ is the density of the medium. Here we assume no body force exists in the medium. We know the stress-displacement relation

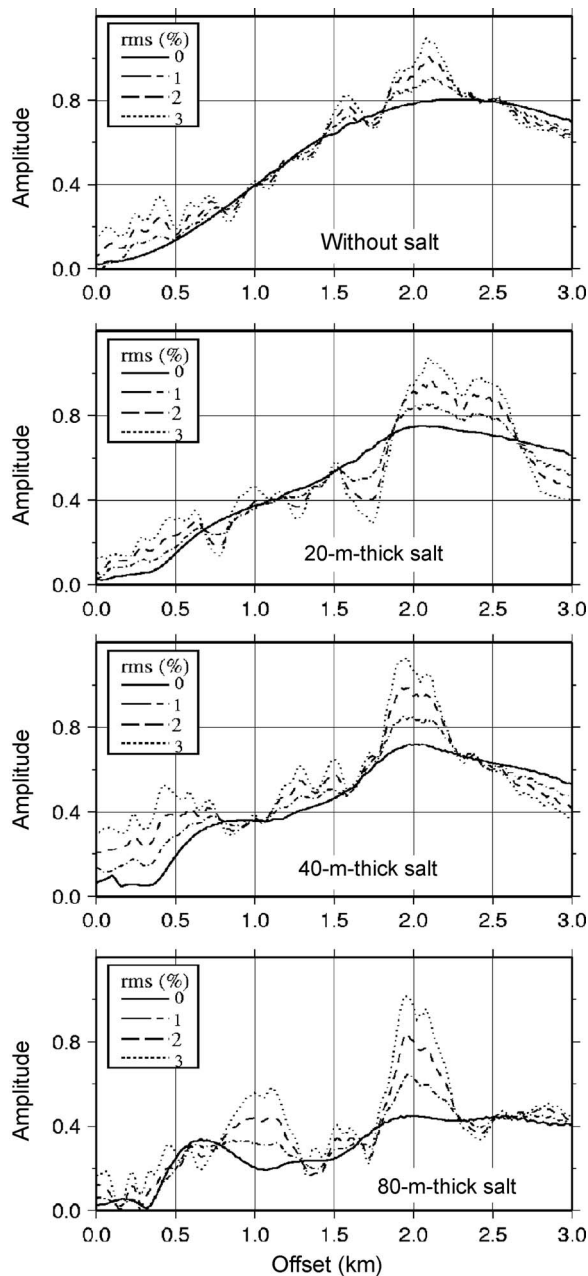


Figure 10. AVOs of the thin gas layer with the combined effects of lateral structure variation and random heterogeneities.

$$\sigma(\mathbf{x}) = \mathbf{c}(\mathbf{x}) : \varepsilon(\mathbf{x}) = \frac{1}{2} \mathbf{c} : (\nabla \mathbf{u} + \mathbf{u} \nabla), \quad (\text{A-2})$$

where \mathbf{c} is the elastic-constant tensor of the medium, ε is the strain field, $\mathbf{u} \nabla$ stands for the transpose of $\nabla \mathbf{u}$, and $:$ stands for double-scalar product of tensors defined through $(\mathbf{ab}) : (\mathbf{cd}) = (\mathbf{b} \cdot \mathbf{c}) \times (\mathbf{a} \cdot \mathbf{d})$. Equation A-1 can then be written as a wave equation of the displacement field:

$$-\omega^2 \rho(\mathbf{x}) \mathbf{u}(\mathbf{x}) = \nabla \cdot \left[\frac{1}{2} \mathbf{c} : (\nabla \mathbf{u} + \mathbf{u} \nabla) \right]. \quad (\text{A-3})$$

If the parameters of the elastic medium and the total wavefield can be decomposed as

$$\begin{aligned} \rho(\mathbf{x}) &= \rho_0 + \delta\rho(\mathbf{x}), \\ \mathbf{c}(\mathbf{x}) &= \mathbf{c}_0 + \delta\mathbf{c}(\mathbf{x}), \\ \mathbf{u}(\mathbf{x}) &= \mathbf{u}^0(\mathbf{x}) + \mathbf{U}(\mathbf{x}), \end{aligned} \quad (\text{A-4})$$

where ρ_0 and \mathbf{c}_0 are the parameters of the background medium, $\delta\rho$ and $\delta\mathbf{c}$ are the corresponding perturbations, \mathbf{u}^0 is the incident field, and \mathbf{U} is the scattered field, then equation A-3 can be rewritten as

$$-\omega^2 \rho_0 \mathbf{U} - \nabla \cdot \left[\frac{1}{2} \mathbf{c}_0 : (\nabla \mathbf{U} + \mathbf{U} \nabla) \right] = \mathbf{F}, \quad (\text{A-5})$$

$$\mathbf{F} = \omega^2 \delta\rho \mathbf{u}(\mathbf{x}) + \nabla \cdot [\delta\mathbf{c}(\mathbf{x}) : \varepsilon(\mathbf{x})], \quad (\text{A-6})$$

where \mathbf{F} is the equivalent body force from scattering.

We can express the scattered displacement field for a thin slab in the horizontal wavenumber domain as

$$\begin{aligned} U(z^*, \mathbf{K}_T) &= \int_{z'}^{z_1} dz \int \int d^2 \mathbf{x}_T \{ \delta\rho \omega^2 u(\mathbf{x}_T, z) \\ &+ \nabla \cdot [\delta\mathbf{c} : \varepsilon(\mathbf{x}_T, z)] \} \cdot G^0(\mathbf{K}_T, z^*; \mathbf{x}_T, z), \end{aligned} \quad (\text{A-7})$$

where

$$\begin{aligned} G^0(z^*, \mathbf{K}_T; z, \mathbf{x}_T) &= \frac{ik_\alpha^2}{2\rho\omega^2} \hat{k}_\alpha \hat{k}_\alpha \frac{1}{\gamma_\alpha} e^{-ik_\alpha r} \\ &+ \frac{ik_\beta^2}{2\omega^2} (\mathbf{I} - \hat{k}_\beta \hat{k}_\beta) \frac{1}{\gamma_\beta} e^{-ik_\beta r}. \end{aligned} \quad (\text{A-8})$$

Here, \mathbf{I} is the unit dyadic and

$$\gamma_\alpha = \sqrt{k_\alpha^2 - K_T^2}$$

and

$$\gamma_\beta = \sqrt{k_\beta^2 - K_T^2}, \quad (\text{A-9})$$

where $k_\alpha = \omega/\alpha$ and $k_\beta = \omega/\beta$ are the P- and S-wavenumbers with α and β as the P- and S-wave velocities, respectively; λ and μ are the Lamé constant. For isotropic media,

$$\delta\mathbf{c}(\mathbf{x}) : \varepsilon(\mathbf{x}) = \delta\lambda(\mathbf{x}) [\varepsilon : \mathbf{I} + 2\delta\mu(\mathbf{x}) \varepsilon(\mathbf{x})]. \quad (\text{A-10})$$

Substituting equation A-8 into equation A-7, we can derive the dual-domain expressions for scattered-displacement fields in isotropic elastic media.

For P-to-P scattering,

$$\begin{aligned} \mathbf{U}^{PP}(\mathbf{K}_T, z^*) &= \frac{ik_\alpha^2}{2\gamma_\alpha} \int_{z'}^{z_1} dz e^{ik_\alpha^2(z^*-z)} \left\{ \hat{k}_\alpha \hat{k}_\alpha \cdot \int \int d^2 \mathbf{x}_T \right. \\ &\times e^{-i\mathbf{K}_T \cdot \mathbf{x}_T} \frac{\delta\rho(\mathbf{x}_T, z)}{\rho} \mathbf{u}_\alpha^0(\mathbf{x}_T, z) \\ &- \hat{k}_\alpha \int \int d^2 \mathbf{x}_T e^{-i\mathbf{K}_T \cdot \mathbf{x}_T} \frac{\delta\lambda(\mathbf{x}_T, z)}{\lambda + 2\mu} \frac{1}{ik_\alpha} \\ &\times \nabla \cdot \mathbf{u}_\alpha^0(\mathbf{x}_T, z) - \hat{k}_\alpha (\hat{k}_\alpha \hat{k}_\alpha) : \int \int d^2 \mathbf{x}_T \\ &\times e^{-i\mathbf{K}_T \cdot \mathbf{x}_T} \frac{\delta\mu(\mathbf{x}_T, z)}{\lambda + 2\mu} \frac{1}{ik_\alpha} \varepsilon_\alpha^0(\mathbf{x}_T, z) \left. \right\}, \end{aligned} \quad (\text{A-11})$$

with $k_z^\alpha = +\gamma_\alpha$ for forescattering, $k_z^\alpha = -\gamma_\alpha$ for backscattering, and $\hat{k}_\alpha = 1/k_\alpha(\mathbf{K}_T, k_z^\alpha)$. In equation A-11, $\mathbf{u}_\alpha^0(\mathbf{x}_T, z)$, $\nabla \cdot \mathbf{u}_\alpha^0(\mathbf{x}_T, z)$, and $\varepsilon_\alpha^0(\mathbf{x}_T, z)$ can be calculated by

$$\begin{aligned} \mathbf{u}_\alpha^0(\mathbf{x}_T, z) &= \frac{1}{4\pi^2} \int \int d^2 \mathbf{K}'_T e^{i\mathbf{K}'_T \cdot \mathbf{x}_T} \mathbf{u}_\alpha^0(\mathbf{K}'_T) e^{i\gamma'_\alpha(z-z')}, \\ \frac{1}{ik_\alpha} \nabla \cdot \mathbf{u}_\alpha^0(\mathbf{x}_T, z) &= \frac{1}{4\pi^2} \int \int d^2 \mathbf{K}'_T e^{i\mathbf{K}'_T \cdot \mathbf{x}_T} \hat{k}'_\alpha \cdot \mathbf{u}_\alpha^0(\mathbf{K}'_T) \\ &\times e^{i\gamma'_\alpha(z-z')}, \end{aligned}$$

$$\begin{aligned} \frac{1}{ik_\alpha} \varepsilon_\alpha^0(\mathbf{x}_T, z) &= \frac{1}{4\pi^2} \int \int d^2 \mathbf{K}'_T e^{i\mathbf{K}'_T \cdot \mathbf{x}_T} \frac{1}{2} [\hat{k}'_\alpha \mathbf{u}_\alpha^0(\mathbf{K}'_T) \\ &+ \mathbf{u}_\alpha^0(\mathbf{K}'_T) \hat{k}'_\alpha] e^{i\gamma'_\alpha(z-z')}, \\ &= \frac{1}{4\pi^2} \int \int d^2 \mathbf{K}'_T e^{i\mathbf{K}'_T \cdot \mathbf{x}_T} \hat{k}'_\alpha \hat{k}'_\alpha \mathbf{u}_\alpha^0(\mathbf{K}'_T) e^{i\gamma'_\alpha(z-z')}, \end{aligned}$$

where $u_\alpha^0(\mathbf{K}'_T) = |\mathbf{u}_\alpha^0(\mathbf{K}'_T)|$ and $\hat{k}'_\alpha = 1/k_\alpha(\mathbf{K}'_T, \gamma'_\alpha)$.

For P-to-S scattering,

$$\begin{aligned} \mathbf{U}^{PS}(\mathbf{K}_T, z^*) &= \frac{ik_\beta^2}{2\gamma_\beta} \int_{z'}^{z_1} dz e^{ik_\beta^2(z^*-z)} \\ &\times \left\{ (\mathbf{I} - \hat{k}_\beta \hat{k}_\beta) \cdot \int \int d^2 \mathbf{x}_T \right. \\ &\times e^{-i\mathbf{K}_T \cdot \mathbf{x}_T} \frac{\delta\rho(\mathbf{x}_T, z)}{\rho} \mathbf{u}_\alpha^0(\mathbf{x}_T, z) \\ &- (\mathbf{I} - \hat{k}_\beta \hat{k}_\beta) \cdot \left[\hat{k}_\beta \cdot \int \int d^2 \mathbf{x}_T \right. \\ &\times e^{-i\mathbf{K}_T \cdot \mathbf{x}_T} \frac{\delta\mu(\mathbf{x}_T, z)}{\mu} \frac{1}{ik_\beta} \varepsilon_\alpha^0(\mathbf{x}_T, z) \left. \right] \left. \right\}, \end{aligned} \quad (\text{A-12})$$

where $\hat{k}_\beta = 1/k_\beta(\mathbf{K}_T, k_z^\beta)$.

For S-to-P scattering,

$$\begin{aligned}
\mathbf{U}^{SP}(\mathbf{K}_T, z^*) &= \frac{ik_\alpha^2}{2\gamma_\alpha} \int_{z'}^{z_1} dz e^{ik_\alpha^2(z^*-z)} \left\{ \hat{k}_\alpha \hat{k}_\alpha \cdot \int \int d^2\mathbf{x}_T \right. \\
&\times e^{-i\mathbf{K}_T \cdot \mathbf{x}_T} \frac{\delta\rho(\mathbf{x}_T, z)}{\rho} \mathbf{u}_\beta^0(\mathbf{x}_T, z) \\
&- (k_\alpha/k_\beta) \hat{k}_\alpha (\hat{k}_\alpha \hat{k}_\alpha) : \int \int d^2\mathbf{x}_T \\
&\times \left. e^{-i\mathbf{K}_T \cdot \mathbf{x}_T} \frac{\delta\mu(\mathbf{x}_T, z)}{\mu} \frac{1}{ik_\beta} \varepsilon_\beta^0(\mathbf{x}_T, z) \right\}. \tag{A-13}
\end{aligned}$$

For S-to-S scattering,

$$\begin{aligned}
\mathbf{U}^{SS}(\mathbf{K}_T, z^*) &= \frac{ik_\beta^2}{2\gamma_\beta} \int_{z'}^{z_1} dz e^{ik_\beta^2(z^*-z)} \left\{ (\mathbf{I} - \hat{k}_\beta \hat{k}_\beta) \cdot \int \int d^2\mathbf{x}_T \right. \\
&\times e^{-i\mathbf{K}_T \cdot \mathbf{x}_T} \frac{\delta\rho(\mathbf{x}_T, z)}{\rho} \mathbf{u}_\beta^0(\mathbf{x}_T, z) - (\mathbf{I} - \hat{k}_\beta \hat{k}_\beta) \\
&\cdot \left[\hat{k}_\beta \cdot \int \int d^2\mathbf{x}_T e^{-i\mathbf{K}_T \cdot \mathbf{x}_T} \frac{\delta\mu(\mathbf{x}_T, z)}{\mu} \right. \\
&\times \left. \left. \frac{1}{ik_\beta} \varepsilon_\beta^0(\mathbf{x}_T, z) \right] \right\}. \tag{A-14}
\end{aligned}$$

In equations A-13 and A-14, $\mathbf{u}_\beta^0(\mathbf{x}_T, z)$ and $\varepsilon_\beta^0(\mathbf{x}_T, z)$ can be calculated by

$$\begin{aligned}
\mathbf{u}_\beta^0(\mathbf{x}_T, z) &= \frac{1}{4\pi^2} \int \int d^2\mathbf{K}'_T e^{i\mathbf{K}'_T \cdot \mathbf{x}_T} \mathbf{u}_\beta^0(\mathbf{K}'_T) e^{i\gamma'_\beta(z-z')} \\
\frac{1}{ik_\beta} \varepsilon_\beta^0(\mathbf{x}_T, z) &= \frac{1}{4\pi^2} \int \int d^2\mathbf{K}'_T e^{i\mathbf{K}'_T \cdot \mathbf{x}_T} \frac{1}{2} [\hat{k}'_\beta \mathbf{u}_\beta^0(\mathbf{K}'_T) \\
&+ \mathbf{u}_\beta^0(\mathbf{K}'_T) \hat{k}'_\beta] e^{i\gamma'_\beta(z-z')},
\end{aligned}$$

where $\hat{k}'_\beta = 1/k_\beta(\mathbf{K}'_T, \gamma'_\beta)$.

REFERENCES

- Adriansyah, and G. A. McMechan, 1998, Effects of attenuation and scattering on AVO measurements: *Geophysics*, **63**, 2025–2034.
- Aki, K., and P. Richards, 1980, *Quantitative seismology: Theory and methods*, vol. 1: W.H. Freeman & Co.
- Bakke, N. E., and B. Ursin, 1998, Thin-bed AVO effects: *Geophysical Prospecting*, **46**, 571–587.
- Chang, H., and G. A. McMechan, 1996, Numerical simulation of multi-parameter scattering: *Bulletin of the Seismological Society of America*, **86**, 1820–1829.
- Chung, H. M., and D. C. Lawton, 1995, Amplitude responses of thin-beds: Sinusoidal approximation versus Ricker approximation: *Geophysics*, **60**, 223–230.
- Dey-Sarkar, S. K., and S. V. Svatek, 1993, Prestack analysis — An integrated approach for seismic interpretation in clastic basin, *in* J. P. Castagna and M. M. Backus, eds., *Offset dependent reflectivity: Theory and practice of AVO analysis: SEG Investigations in Geophysics*, **8**, 57–77.
- Garcia, A. I., and M. M. Backus, 1985, Thin-layer response catalog: 57th Annual International Meeting, SEG, Expanded Abstracts, 614–616.
- Gregory, A. R., 1977, Aspects of rock physics from laboratory and log data that are important to seismic interpretation, *in* C. E. Payton, ed., *Seismic stratigraphy — Applications to hydrocarbon exploration: AAPG Memoir* **26**, 15–46.
- Huang, L. J., M. C. Fehler, P. M. Roberts, and C. C. Burch, 1999a, Extended local Rytov Fourier migration method: *Geophysics*, **64**, 1535–1545.
- Huang, L. J., M. C. Fehler, and R. S. Wu, 1999b, Extended local Born Fourier migration method: *Geophysics*, **64**, 1524–1534.
- Jin S., R. S. Wu, and C. Peng, 1999, Seismic depth migration with screen propagators: *Computational Geoscience*, **3**, 321–335.
- Kang, I. B., and G. A. McMechan, 1994, Separation of intrinsic and scattering Q based on frequency-dependent amplitude ratios of transmitted waves: *Journal of Geophysical Research*, **99**, 23875–23885.
- Simmons, J. L., and M. M. Backus, 1994, AVO modeling and the locally converted shear wave: *Geophysics*, **59**, 1237–1248.
- Wapenaar, K., A. J. van Wijngaarden, W. van Geloven, and E. van der Leij, 1999, Apparent AVO effects of fine layering: *Geophysics*, **64**, 1939–1948.
- Widess, M. B., 1973, How thin is a thin-bed?: *Geophysics*, **38**, 1176–1180.
- Wild, J., and J. A. Hudson, 1998, A geometrical approach to the elastic complex screen: *Journal of Geophysical Research*, **103**, 707–726.
- Wu, R. S., 1994, Wide-angle elastic wave one-way propagator in heterogeneous media and an elastic wave complex-screen method: *Journal of Geophysical Research*, **99**, 751–766.
- , 1996, Synthetic seismograms in heterogeneous media by one-return approximation: *Pure and Applied Geophysics*, **148**, 155–173.
- Wu, R. S., and K. Aki, 1985, Scattering characteristics of elastic waves in an elastic heterogeneity: *Geophysics*, **50**, 582–595.
- Wu, R. S., and L. J. Huang, 1995, Reflected wave modeling in heterogeneous acoustic media using De Wolf approximation, *in* *Mathematical methods in geophysical imaging III: SPIE Proceedings Series*, **2571**, 176–193.
- Wu, R. S., and S. Jin, 1997, Windowed GSP (generalized screen propagators) migration applied to SEG-EAEG salt model data: 67th Annual International Meeting, SEG, Expanded Abstracts, 1746–1749.
- Wu, R. S., S. Jin, and X. B. Xie, 2000a, Energy partition and attenuation L_g waves by numerical simulations using screen propagators: *Physics of the Earth and Planetary Interiors*, **120**, 227–244.
- , 2000b, Seismic wave propagation and scattering in heterogeneous crustal waveguides using screen propagators: I, SH waves: *Bulletin of the Seismological Society of America*, **90**, 401–413.
- Wu, X. Y., and R. S. Wu, 1999, Wide-angle thin-slab propagator with phase matching for elastic modeling: 69th Annual International Meeting, SEG, Expanded Abstracts, 1867–1870.
- , 2001, L_g -wave simulation in heterogeneous crusts with surface topography using screen propagators: *Geophysical Journal International*, **146**, 670–678.
- Xie, X. B., and R. S. Wu, 2001, Modeling elastic wave forward propagation and reflection using the complex-screen method: *Journal of the Acoustical Society of America*, **109**, 2629–2635.
- , 2005, Multicomponent prestack depth migration using the elastic screen method: *Geophysics*, **70**, S30–S37.
- Yilmaz, Ö., 1987, *Seismic data processing: SEG Investigations in Geophysics*, **2**.
- Youn, O. K., H. Zhou, and R. E. Sheriff, 1998, Structural effects on AVO: A modeling study: 68th Annual International Meeting, SEG, Expanded Abstracts, 197–200.